Finite Horizon Analysis of Autolanded Aircraft in Final Approach under Crosswind⋆

Felix Biertümpfel*, Harald Pfifer

Chair of Flight Mechanics and Control, Technische Universität Dresden, 01069 Dresden, Germany

ARTICLE INFO

Keywords:
Robust Control
Linear Time Varying Systems
Integral Quadratic Constraints
Aircraft Control
Aerospace Applications

ABSTRACT

The paper presents a worst-case touchdown performance analysis of auto-landed aircraft under complex wind disturbance. It takes advantage of the fact that the approaching aircraft effectively follows a predefined trajectory provided by the instrument landing system. Thus, the aircraft dynamics' linearization along the approach trajectory results in a finite horizon linear time-varying (LTV) representation. This naturally allows to include altitude triggered control law changes and changes in the flight dynamics, e.g., due to ground effect, in the analysis. To cover a broad range of environmental and aircraft parameter combinations in the worst-case analysis, a time-varying trajectory uncertainty description is introduced. The uncertainty's input/output behavior is covered by integral quadratic constraints. Thus, recent advances on the worst-case gain analysis of finite horizon LTV systems can be used. The corresponding analysis condition is based on a parameterized Riccati differential equation's solvability, which leads to a readily solvable nonlinear optimization problem. Applying the robust LTV framework, worst-cases for common touchdown criteria, such as vertical touchdown velocity, are calculated. These worst-cases cover the influence of complex wind fields and a large aircraft and environmental parameter set. The results are evaluated against corresponding Monte Carlo simulation on the original high fidelity, industry-sized nonlinear aircraft model.

1. Introduction

More than 60% of all accidents in civil aviation history occurred during approach or landing rendering them the most safety critical flight phases by some margin [2, 8]. Over the last two decades, the mandatory implementation of autoland systems in airliners reduced the absolute amount of accidents especially for poor visual conditions [13]. Autoland systems are dedicated autopilots designed to track the localizer and glideslope signal of the runway's instrument landing system, perform the touchdown, and decelerate the aircraft on the runway. These systems must operate safely for a large set of aircraft parameters and environmental conditions. Although, highly reliable inside this operating window, their performance deteriorates quickly if (turbulent) wind disturbances start violating this window [1]. This significantly reduces their operational capability in bad weather, e.g., thunder storms. Hence, recent research focuses on the development of control designs increasing the autoland's robustness against wind disturbance [3, 4, 24]. Therefore, it becomes mandatory to develop fast and reliable accompanying worst-case touchdown performance analysis tools for their design and certification process.

Requirements for the capabilities and performance of autoland systems, and their proof of compliance are defined by the aviation authorities such as the European Union Aviation Safety Agency (EASA) or Federal Aviation Administration (FAA). Following for instance the EASA's CS-AWO 131(c) ([9]), the autoland system must satisfy limits on the longitudinal touchdown point, lateral deviation to the centerline, sink rate, bank angle and sideslip angle for a large set of aircraft and environmental parameters, e.g., landing weight, center of gravity, wind conditions and airfield elevations. The autoland's compliance with these specifications must be demonstrated by a combination of analysis and flight test demonstration. Autoland analyses found in literature ([4, 15, 16, 18, 24]) rely solely on simulation-based methods such as Monte Carlo simulations or worst-case optimizations of the nonlinear aircraft model covering reasonable combinations of the parameters defined in [9]. These methods are computationally expensive, as they must cover extensive aircraft and environmental conditions, and disturbances. Moreover, due to the sample-based nature, they are limited to provide lower bounds to the actual worst-case performance, e.g., a lower bound on the maximum sink rate at touchdown ([4, 18, 24]). In case of Monte Carlo based methods, additional probabilistic statements are possible if a suitable probability distribution can be fitted into the performance metric, e.g., confidence intervals or the probability of exceedance regarding certification bounds for the predicted sink rate at touchdown.

In contrast to these classical lower bound methods, recently several worst-case analysis methods based on the linear time-varying (LTV) integral quadratic constraint (IQC) framework have been proposed, see e.g., [7, 22]. In short, these methods are based on an extension of the bounded real lemma (BRL) for LTV systems to cover integral quadratic constraints [22]. Reference [7] then proposed an efficient worst-case optimization framework to solve the BRL conditions over large time horizons.

The present paper contributes a guaranteed worst-case analysis of typical touchdown constraints under crosswind conditions for a complex benchmark aircraft with an au-

⋆Conflict of interest - none declared

*Corresponding author

felix.biertuempfel@tu-dresden.de (F. Biertümpfel); harald.pfifer@tu-dresden.de (H. Pfifer)

ORCID(s):

tolanding system. A major focus of the paper is put on the realism of the analysis scenario. As such, the considered uncertainties, disturbances and performance metrics of the analysis are chosen in accordance with the EASA certification requirements for automatic landing systems (CS-AW0 131 Performance Demonstration). The approach exploits the fact that during automated landing, the aircraft follows a predefined trajectory based on the glideslope and localizer signal of the instrument landing system (ILS). Hence, the aircraft's dynamic can be represented as an explicit time-varying system along the approach trajectory. A Jacobian-based linearization along the trajectory leads to finite horizon linear time-varying (LTV) system which can be used in the LTV-IQC framework to perform worst-case analyses. The proposed method is based on a recent extension of the bounded real lemma (BRL) for LTV systems to cover integral quadratic constraints in [22] and a worst-case optimization framework in [7]. The optimization framework allows for an efficient analysis of large-scale LTV systems over long horizons, covering various types of perturbations such as real parametric and dynamic uncertainties. Its feasibility was demonstrated in an industry relevant worst-case loads analysis of a space launcher under atmospheric disturbance in [6]. The theoretic and computational preliminaries are given in Section 2. In summary, the proposed analysis supplements classical probability based tools for approach analyses by providing fast guaranteed worst-case results. Due to the computational efficiency of the method, it can be easily integrated in an iterative control design loop.

The benchmark aircraft considered in this paper is a large twin-engine airliner comparable to an Airbus A330. The model was introduced in [4] and is freely available from `https://w3.onera.fr/smac/aircraftModel`. It was used in an auto-landing control design challenge formulated in [3]. As part of the challenge a fully functional robust control design was developed in [24]. Both the aircraft model and the controller are briefly described in Section 3. The novel benchmark analysis presented in Section 4 is a worst-case touchdown analysis of the controller ([24]) under wind disturbances. The evaluated touchdown criteria are directly taken from the design challenge [3]. The worst-case analysis is compared to results from nonlinear Monte Carlo simulations.

A special focus in the present paper is put on the accurate treatment of wind scenarios in the proposed worst-case framework. Two different types of wind disturbances are considered in the analysis: Altitude dependent wind fields and turbulence. The former can be directly treated in the calculation of the reference trajectory. The latter is, however, more complicated. Since the LTV-IQC framework is based on induced norm metrics, a corresponding time horizon dependent shaping filter is designed. This approach is along the lines of similar methods for time invariant or parameter varying systems in literature, see, e.g., [12, 14, 17].

2. Background on Finite Horizon Robustness Analysis

A finite horizon continuous LTV system G_t is defined as

$$\begin{aligned} \dot{x}_t(t) &= A_t(t)\, x_t(t) + B_t(t)\, d(t) \\ e(t) &= C_t(t)\, x_t(t) + D_t(t)\, d(t), \end{aligned} \tag{1}$$

where $x_t(t) \in \mathbb{R}^{n_{x_t}}$ denotes the state vector, $d(t) \in \mathbb{R}^{n_d}$ the input vector, and $e(t) \in \mathbb{R}^{n_e}$ the output vector. Its system matrices are locally bounded continuous functions of time t and compatible size-wise to the corresponding vectors, e.g., $A_t(t) \in \mathbb{R}^{n_{x_t} \times n_{x_t}}$. The explicit time dependency will be omitted regularly to shorten the notation. The finite horizon Lebesgue 2-norm $L_2[0,T]$ is used to describe the size of a signal $d(t)$ in this paper [23]:

$$\|d\|_{2[0,T]} = \sqrt{\int_0^T d(t)^T d(t)\, dt}. \tag{2}$$

2.1. Integral Quadratic Constraints

In this paper, the input/output behavior of an uncertainty Δ is bounded via IQCs. The IQC time-domain definition is based upon a filter $\Psi \in \mathbb{RH}_\infty^{n_z \times (n_v + n_w)}$ and an $n_z \times n_z$ real, symmetric matrix M [20, 21]. A graphical interpretation is given in Fig. 1. The uncertainty Δ satisfies the IQC defined

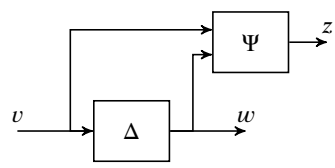

Figure 1: Time-domain IQC interpretation of the uncertainty Δ

by M and Ψ if the filter Ψ's output z resulting from filtering the uncertainty input v and output w fulfills the quadratic time constraint

$$\int_0^T z(t)^T M z(t)\, dt \geq 0 \tag{3}$$

for all $v \in L_2[0,T]$ and $w = \Delta(v)$ over the finite-horizon $[0,T]$. If satisfied, the short notation $\Delta \in IQC(\Psi, M)$ is used.

2.2. Robust Finite Horizon Analysis Condition

A robust performance analysis framework, can be derived from the worst-case analysis condition of nominal LTV systems in [10] and the time-domain IQC representation of the uncertainty Δ [5, 22]. It covers the feedback interconnection $F_u(G_t, \Delta)$ of a known LTV system G_t and an uncertainty Δ satisfying an IQC described by Ψ and M, i.e. $\Delta \in IQC(\Psi, M)$. Thus, the IQC filter Ψ can be connected to the feedback interconnection as shown in Fig. 2. The resulting extended LTV system G's dynamics are defined by

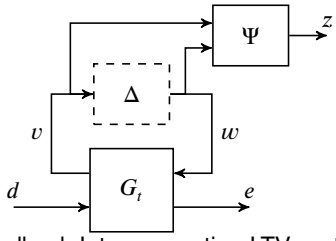

Figure 2: Feedback Interconnection LTV system G_t and uncertainty Δ

$$\begin{aligned} \dot{x}(t) &= A(t)\,x(t) + [\,B_1(t)\;\; B_2(t)\,]\begin{bmatrix} w(t) \\ d(t) \end{bmatrix} \\ \begin{bmatrix} z(t) \\ e(t) \end{bmatrix} &= \begin{bmatrix} C_1(t) \\ C_2(t) \end{bmatrix} x(t) + \begin{bmatrix} D_{11}(t) & D_{12}(t) \\ D_{21}(t) & D_{22}(t) \end{bmatrix}\begin{bmatrix} w(t) \\ d(t) \end{bmatrix}, \end{aligned} \tag{4}$$

with the state vector $x(t) \in \mathbb{R}^{n_x}$ consisting of G_t's and Ψ's states, the input vector $d(t) \in \mathbb{R}^{n_d}$, and the output vector $e(t) \in \mathbb{R}^{n_e}$. Hence, the time-domain inequality (3) enforced on the IQC filter output z replaces the explicit uncertainty representation $w = \Delta(v)$.

The finite horizon worst-case $L_2[0,T]$ to $\|e(T)\|_2$ gain presents an applicable performance metric to quantify the touchdown constraints. It is defined as:

$$\|F_u(G_t,\Delta)\|_2 := \sup_{\Delta\in \mathrm{IQC}(\Psi,M)} \; \sup_{\substack{d\in L_2[0,T] \\ d\neq 0, x(0)=0}} \frac{\|e(T)\|_2}{\|d(t)\|_{2[0,T]}}. \tag{5}$$

It geometrically describes the ball upper bounding the worst-case output $e(T)$ at the final time T over all $\Delta \in IQC(\Psi, M)$ for $\|d(t)\|_{2[0,T]} \leq 1$.

A dissipation inequality defining an upper bound on the worst-case $L_2[0,T]$ to $\|e(T)\|_2$ gain of the interconnection $F_u(G_t,\Delta)$ can be derived based on the extended system G (4) and the IQC (3) ([7, 22]). This dissipation inequality leads to a linear matrix inequality, which can be stated equivalently as an integrability condition of a Riccati differential equation (RDE). The latter is given in Theorem 1([7, 22]).

Theorem 1. *Let $F_u(G_t,\Delta)$ be well posed $\forall\,\Delta \in IQC(\Psi, M)$, then $\|F_u(G_t,\Delta)\|_2 < \gamma_{WC}$ if there exists a continuously differentiable symmetric $P : [0,T] \to \mathbb{R}^{n_x\times n_x}$ such that*

$$P(T) = \frac{1}{\gamma_{WC}} C_2(T)^T C_2(T), \tag{6}$$

$$\dot{P} = Q + P\tilde{A} + \tilde{A}^T P - PSP \qquad \forall t \in [0,T], \tag{7}$$

and

$$R = \begin{bmatrix} D_{11}^T M D_{11} & D_{11}^T M D_{12} \\ D_{12}^T M D_{11} & D_{12}^T M D_{12} - \gamma_{WC} I \end{bmatrix} < 0 \,\forall\, t \in [0,T], \tag{8}$$

with

$$\tilde{A} = [\,B_1\;\; B_2\,]\, R^{-1} \begin{bmatrix} (C_1^T M D_{11})^T \\ (C_1^T M D_{12})^T \end{bmatrix} - A, \tag{9}$$

$$S = -[\,B_1\;\; B_2\,]\, R^{-1} \begin{bmatrix} B_1^T \\ B_2^T \end{bmatrix} \tag{10}$$

and

$$Q = -C_1^T M C_1 + \begin{bmatrix} (C_1^T M D_{11})^T \\ (C_1^T M D_{12})^T \end{bmatrix}^T R^{-1} \begin{bmatrix} (C_1^T M D_{11})^T \\ (C_1^T M D_{12})^T \end{bmatrix}. \tag{11}$$

PROOF. The proof builds on the definition of a time dependent quadratic storage function $V(x,t) = x^T P(t) x$. Perturbing (7) results in a Riccati differential inequality which can be reformulated as an LMI using Schur's complement. Multiplying $[x^T, w^T, d^T]$ and $[x^T, w^T, d^T]^T$ on the LMI's left and right side, respectively, gives a dissipation inequality. Integrating this dissipation inequality from 0 to T for zero initial conditions gives

$$\int_0^T z(t)^T M z(t) dt - \gamma \int_0^T d(t)^T d(t) dt + x(T)^T P(T) x(T) < 0. \tag{12}$$

The equality (6) is left and right multiplied with $x(T)^T$ and $x(T)$, respectively, providing

$$x(T)^T P(T) x(T) - \frac{1}{\gamma_{\mathrm{WC}}} e(T)^T e(T) > 0. \tag{13}$$

The substitution of (12) in (13) and subsequently employing the vector 2-norm (Euclidean) $\|e(T)\|_2^2 = e(T)^T e(T)$ results in the upper bound γ_{WC} on (5).

A more detailed proof can be found in [22]. Note that Theorem 1 only provides an upper on the worst-case gain. However, the Theorem does not provide information on the tightness of this bound.

2.3. Computational Approach

In general, a specific Δ can be represented by an infinite amount of IQCs. This problem is generally circumvented in literature by selecting a fixed filter Ψ and freely parameterize M [20, 25]. However, M must be restricted to a feasible set $\mathcal{M}$ such that $\Delta \in IQC(\Psi, M)$ for all $M \in \mathcal{M}$. Consequentially, the RDE (7) in Theorem 1 is parametrized with M. A feasible parametrization for a full-block uncertain LTI dynamic uncertainty is given in Example 1 [25]. It will be applied in the analysis in Section 4.

Example 1. *Let Δ be a full-block dynamic LTI uncertainty, with $\Delta \in \mathbb{RH}^{n_w\times n_v}$ and $0 < \|\Delta\|_\infty \leq b$. A valid time-domain IQC for Δ is defined by $\Psi = \begin{bmatrix} b\psi_\nu \otimes I_{n_v} & 0 \\ 0 & \psi_\nu \otimes I_{n_w} \end{bmatrix}$ and $\mathcal{M} := \{M = \begin{bmatrix} X\otimes I_{n_v} & 0 \\ 0 & -X\otimes I_{n_w} \end{bmatrix} : X = X^T \geq 0 \in \mathbb{R}^{(\nu+1)\times(\nu+1)}\}$. A typical choice for $\psi_\nu \in \mathbb{RH}_\infty^{(\nu+1)\times 1}$ is:*

$$\psi_\nu = \begin{bmatrix} 1 & \frac{1}{(s-\rho)} & \dots & \frac{1}{(s-\rho)^\nu} \end{bmatrix}^T, \; \rho < 0, \; \nu \in \mathbb{N}_0. \tag{14}$$

The basis function ψ_ν with user-selected ν and ρ defines the fixed filter Ψ, whereas X is a free parameter. Hence, a nonlinear optimization problem over M constrained by

the RDE's solvability to minimize the upper bound γ on the worst-case gain can be stated:

$$\begin{aligned} &\min_{M \in \mathcal{M}} \gamma \\ &\text{such that } \forall t \in [0, T] \\ &P(T) = \frac{1}{\gamma_{\mathrm{WC}}} C_2(T)^T C_2(T) \\ &\dot{P} = Q + P\tilde{A} + \tilde{A}^T P - PSP \\ &R < 0 \end{aligned} \tag{15}$$

This nonlinear optimization problem can be readily solved with the algorithm provided in [7]. It combines an inner loop bisecting γ_{WC} for a given M with an outer loop identifying the optimal $M \in \mathcal{M}$ and γ_{WC} by employing the specifically designed meta-heuristic algorithm Log-L-SHADE. This algorithm provides the user with a set of adjustable parameters to tune it to a specific analysis. These incorporate the decision variable search space, the initial population size, i.e. the size of the initial, randomized decision variable set, and the amount of population iterations, i.e., the amount of decision set iterations. As a rule of thumb, the latter two scale with size of IQC parameterization. A detailed discussion of the settings and their respective effects on the search performance is provided in [7].

3. Autolanding Model

The considered aircraft is in a standard nonlinear six-degrees-of-freedom form in a body-fixed frame with translational velocities u, v , and w and angular velocities p, q, and r. The aircraft's orientation in the Earth-fixed frame is given by the standard Euler angles Φ, Θ, and Ψ [19]. The aircraft's center of gravity position in the Earth-fixed frame is denoted by x, y, and z. The path angle γ, course angle χ, and ground speed V_g (horizontal speed relative to earth) define the aircraft's flight path relative to the Earth. Its aerodynamic angle of attack α and sideslip angle β are calculated based on the aerodynamic velocity resulting from superimposing its translational velocity and the atmospheric wind. In approach, the aircraft is controlled by a pair of ailerons, an elevator, a rudder, and symmetrically operating twin engines. First-order low-pass transfer functions are utilized to characterize the actuator dynamics in the simulation. Each actuator is implemented with a specific deflection limit/saturation and rate limit. Note that these limits are only considered in the Monte Carlo simulations and are omitted from LTV worst-case analysis. A standard atmosphere model based on the international standard atmosphere (ISA) is provided to model the effects of different airfield elevations and outside air temperatures.

The autoland controller originally developed in [24] is analyzed in this paper. Only a brief description of the control architecture is provided here with a special focus on the parts of the controller that become explicitly time-dependent along a specific approach trajectory. For a detailed overview of the control design procedure the interested reader is referred to [24]. The control design considers the longitudinal and lateral motion as decoupled. Hence, both motions and the corresponding controllers are analyzed separately in the course of this paper. The controller structure for the longitudinal motion is depicted in Fig. 3 and its implementation for the LTV analysis described in the following paragraphs.

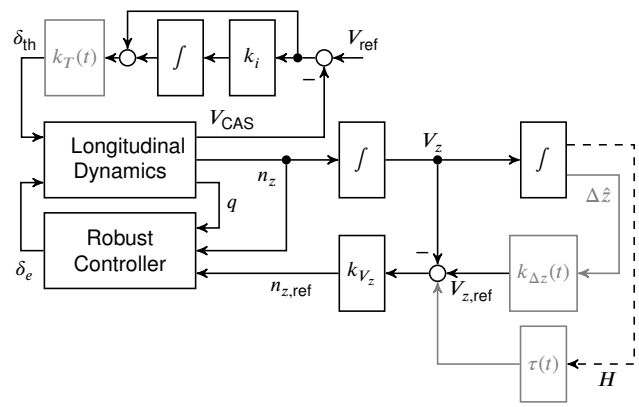

Figure 3: Longitudinal part of the autoland controller as used in the LTV analysis (time-varying gains highlighted)

The auto-throttle maintains the approach speed constant V_{ref} providing a throttle command. It provides a throttle command δ_{th} until flare initiation at a fixed height above ground level $H_{\mathrm{AGL}} = 20\,\mathrm{m}$, which along a specific trajectory corresponds to a time T_{fl}. The auto-throttle is implemented as proportional-integral (PI) controller using calibrated airspeed V_{CAS} feedback:

$$\delta_{\mathrm{th}} = k_T \left(1 + \frac{1}{15}\frac{1}{s}\right)\left(V_{\mathrm{ref}} - V_{\mathrm{CAS}}\right), \tag{16}$$

with $k_T = 0.045$ before flare initiation and 0 after, i.e., K_T is implemented as a time-varying scalar.

The *Robust Controller* block represents a multi-input single-output fifth-order H_∞ controller. It calculates the elevator deflections based on the provided reference load factor $n_{z,\mathrm{ref}}$ and the respective measured signals n_z and q.

The reference load factor $n_{z,\mathrm{ref}}$ is tracked by a proportional sink rate controller:

$$n_{z,\mathrm{ref}} = k_{V_z}(V_{z,\mathrm{ref}} - V_z), \tag{17}$$

with $k_{V_z} = 0.625$. Note that in (17) V_z is the altitude of the landing gear.

The glide slope tracker calculates the reference sink rate signal $V_{z,\mathrm{ref}}$ until initiation of the flare maneuver using a proportional control law:

$$V_{z,\mathrm{ref}} = k_{\Delta z}(t)\Delta\hat{z}, \tag{18}$$

with $k_{\Delta z} = 0.1$ and zero after T_{fl}. Note that offset $\Delta\hat{z}$ describes the landing gear's deviation from the centerline.After flare initiation, i.e., $t \geq T_{\mathrm{fl}}$, a dedicated flare controller provides the $V_{z,\mathrm{ref}}$ signal to the sink rate tracker. Therefore, the feedback loop from H_{AGL} to V_z is closed via

$$V_{z,\mathrm{ref}} = \tau(H_{\mathrm{AGL}} + H_{\mathrm{bias}}). \tag{19}$$

The gain τ as well as H_{bias} (calculated offset value) are zero before flare initialization T_{fl} and depend afterwards on the sink rate at $t = T_{\text{fl}}$ and the desired vertical velocity at touchdown. Reference [24] elaborates the calculation procedure. As the sink rate at flare initialization depends on the approach scenario (wind cases, aircraft parameters, etc.), the values of τ vary in a range from 4.6 to 12.3 in the worst-case analysis. For the nominal trajectory under headwind the value of τ is 8.38 and under tailwind 6.26.

The lateral controller's structure is depicted in Fig. 4. The lateral directional control is provided by a ninth-order

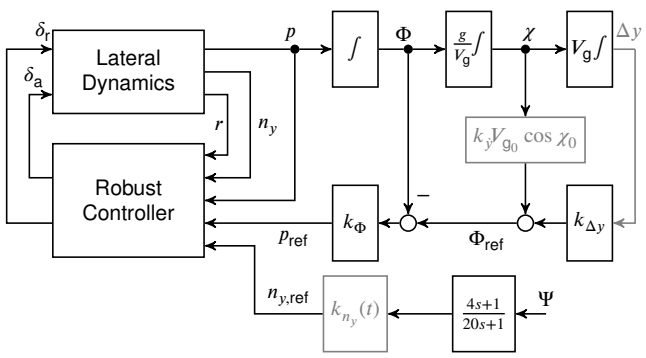

Figure 4: Lateral part of the autoland controller as used in the LTV analysis (adaptations highlighted)

multivariable H_∞ controller using roll rate and lateral load factor feedback represented by the *Robust Controller* block.

A bank angle tracker calculates the H_∞ controller's reference roll rate using proportional bank angle feedback:

$$p_{\text{ref}} = k_\phi \left(\phi_{\text{ref}} - \phi\right), \tag{20}$$

with $k_\phi = 0.7$.

The reference bank angle in (20) is calculated by the localizer signal tracker. The controller approximates $\Delta\dot{y}$ as $\Delta\dot{y} \approx V_g \sin\chi$ resulting in the following controller:

$$\phi_{\text{ref}} = k_{\Delta y}\Delta\hat{y} + k_{\dot{y}} V_g \sin\chi, \tag{21}$$

with $k_{\Delta y} = 0.003$ and $k_{\dot{y}} = 0.033$. The signal $\Delta\hat{y}$ provides the landing gear's offset to the centerline rather than the sensor's offset Δy. Equation (21) is nonlinear in χ and requires a linearization along the approach trajectory for the LTV analysis. Fig. 4 emphasizes this adaptation.

The decrab maneuver is initiated at a fixed height above ground level $H_{\text{AGL}} = 5$m, which along a specified trajectory corresponds to the time T_{DC}. The decrab controller is given as:

$$n_{y,\text{ref}} = k_{n_y}(t)\frac{4s+1}{20s+1}\psi, \tag{22}$$

with $k_{n_y} = 33$ after initiation of the decrab maneuver and zero otherwise.

3.1. Performance Metrics and Disturbances

The autoland controller's performance is evaluated with respect to five touchdown criteria, which are specified by the

Table 1
Touchdown performance criteria

$V_{z,\text{TD}}$ [m/s]	H_{60} [m]	$y_{\text{LG,TD}}$ [m]	ϕ_{TD} [deg]	$\beta_{\text{LG,TD}}$ [deg]
6.2	0	15	12	14

certification authorities, e.g., the EASA ([9]) or the FAA. Firstly, the vertical speed at touchdown $V_{z,\text{TD}}$ which indicates hard landings, i.e. exceeding the main landing gears structural limit load. Secondly, the height of the main landing gear above runway 60m behind the runway threshold H_{60}, which if zero indicates a short landing. Thirdly, the lateral deviation from the runway centerline at touchdown $y_{\text{LG,TD}}$ indicating the risk of a runway excursion. The penultimate criterion is the bank angle at touchdown ϕ_{TD} evaluating the risk of a wingtip strike. The final criterion is the landing gear sideslip angle relative to the centerline at touchdown $\beta_{\text{LG,TD}}$ assessing the structural load on the landing gear. Recommendations for the limit of the each criterion are provided in [3] for the given aircraft and summarized in Tab. 1. These limits have to be satisfied for a set of aircraft and environmental parameters. A set satisfying the requirements defined in the CS-AWO is derived in [3] and summarized in Tab. 2. The aircraft parameter include the minimum and maximum touchdown mass and center of mass. The touchdown mass mainly influences the aircraft inertias. Higher masses make the aircraft more sluggish to control commands. Lower masses make it more sensible to wind. The center of mass directly influence the aircrafts stability. The environmental requirements are based on statistical evaluations of existing airports. A specifically critical environment combination is a high runway elevation and high temperature, resulting in low lift and reduced control authority. In addition, the autoland system must satisfy the performance criteria under complex wind disturbances including wind shears and turbulence.

3.2. Linear Time-Varying Dynamics

The general LTV representation G_t of the aircraft is derived by Jacobian-based linearization of the nonlinear model along a nominal approach trajectory. This trajectory is obtained by simulation of a reference approach with the aircraft and approach scenario in the following setting. The aircraft's center of gravity position is at 22% of the mean aerodynamic chord and it has a mass of 140 t. The reference airfield is at mean sea level under nominal ISA condition. Finally, the approach starts at 300 m altitude, 30 m below the glide slope and 20 m right of the localizer signal.

The cross-coupling between the longitudinal and lateral motion is neglectable during the approach. This assumption is justified by the small bank and pitch angles during approach following from the control design and trajectory. Moreover, the longitudinal and lateral aerodynamics in the nonlinear model are not coupled through the angle of attack and the sideslip angle. For more details see [3] or [24].

Table 2
Aircraft and environmental parameters of the nonlinear model

Parameter	Distribution*	min	max
Mass $[t]$	uniform	120	180
Center of mass $[\%]$	uniform	15	41
Temperature $[°C]$	uniform	−69	40
Runway slope $[\%]$	$\mathcal{N}(0, 0.4)$	−2	2
Glide Slope [deg]	$\mathcal{N}(-3, 0.075)$	−3.15	−2.85
Runway elevation [ft]	$[-1000, 250]$: 50%	−1000	9200
	$[250, 750]$: 28.33%		
	$[750, 1250]$: 13.33%		
	$[1250, 1750]$: 3.33%		
	$[1750, 2500]$: 1.67%		
	$[2500, 3500]$: 1.00%		
	$[3500, 4500]$: 0.67%		
	$[4500, 9200]$: 1.67%		

*$\mathcal{N}(\mu, \sigma)$: normal distribution with mean μ and standard deviation σ.

Hence, separate models for the longitudinal and lateral analysis can be derived from G_t. The longitudinal analysis interconnection consisting of the respective controller and aircraft dynamics $G_{\text{long,nom}}$ has 17 states, two disturbance inputs (i.e., longitudinal wind u_{w} and vertical wind w_{w}) and two performance outputs (i.e., sink rate $V_{z,\text{LG}}$ and height above ground H_{LG}). The lateral analysis interconnection $G_{\text{lat,nom}}$ has 19 states, lateral wind v_{w} as single disturbance input, and three performance outputs, namely lateral offset to centerline, wheel sideslip β_{LG} and bank angle.

As a result of the different phases of the approach, i.e., tracking and flare segment, the aircraft possesses noticeably time-varying dynamics. This characteristic is exemplary shown by the bode magnitude plot in Fig. 5. It depicts the transfer function from δ_{e} to α calculated on frozen points in time corresponding to a landing gear altitude interval from 50 m to 0 m with a step size of 2.5 m along the nominal approach trajectory. A significant change in the dynamics occurs as soon as the flare is triggered. Hence, the transfer functions after flare initialization are colored in light blue (——).

3.3. Wind Model

The wind disturbances analyzed in this paper are derived from [3], which are based on the EASA certification requirements for autoland systems [9]. They were also applied in [24] for the controller design verification. They consist of a turbulent wind field added to an altitude-dependent wind shear. The resulting wind profiles are used to design a corresponding LTV wind model for the worst-case analysis.

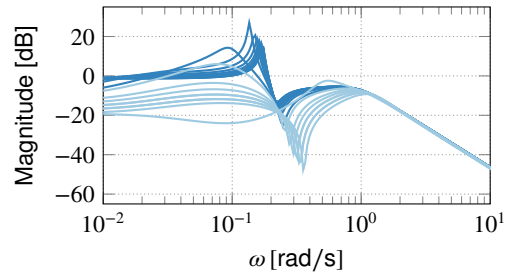

Figure 5: Bode magnitude plot of δ_{e} to α transfer function evaluated at frozen points in time covering the approach trajectory from 50 m to 0 m: Before flare initiation (——), after flare initiation (——)

3.3.1. *Steady Wind*

Two distinct steady wind fields are considered in the analysis. The first consists of a tail and crosswind component w_{tail} and w_{cross}, respectively, with altitude dependent magnitudes. They both reach their maximum magnitudes of 10 kts and 25 kts, respectively, 15 m above the ground. These wind magnitudes correspond to the maximum values expected in [3] and are chosen to account for the worst-case type analysis in the present paper. Their build-up follows the same description, which is shown on the example of w_{tail}:

$$\begin{aligned} w_{\text{tail}} =& 10\,\text{kts}\left(\frac{1}{2}\frac{(H_{\text{AGL}} - H_{\text{AGL,0}})^2}{(H_{\text{AGL,0}} - 15\,\text{m})^2} + 1\right) \\ &- 10\,\text{kts}\left(\frac{1}{2}\left|\frac{(H_{\text{AGL}} - H_{\text{AGL,0}})^2}{(H_{\text{AGL,0}} - 15\,\text{m})^2} - 1\right|\right), \end{aligned} \tag{23}$$

where $H_{\text{AGL,0}}$ is the aircraft's initial altitude. Similarly, altitude dependent head- and crosswind components with maximum magnitudes of 30 kts and 25 kts, respectively, form the second wind field. Note that knots are used often in this paper as the unit for velocities, as is still very common in aeronautics.

As a consequence of their altitude dependence, the constant wind profiles are unique for a specific trajectory. Hence, the LTV model derived from a reference trajectory calculated for a given wind scenario implicitly includes the latter's influence on the aircraft dynamics.

3.3.2. *Turbulent Wind*

In case of the longitudinal touchdown conditions simultaneous longitudinal and vertical turbulence is added to the two steady wind fields described above. The longitudinal turbulence is generated by filtering a random number signal with zero mean, variance of one, and sample time of 0.05 s through the first-order filter G_{u_w} described by

$$G_{u_{\text{w}}} = \frac{116}{2.5s + 1}. \tag{24}$$

The vertical turbulence is formed by the same type of random signal passed through the first-order filter G_{w_w}:

$$G_{w_{\text{w}}} = \frac{3.375}{0.125s + 1}. \tag{25}$$

Lateral turbulence is added to the (two) steady wind fields to analyze the lateral touchdown conditions. This lateral turbulence field is generated in the same way as longitudinal one. Note that the filters G_{u_w} and G_{w_w} are shaping filters with low pass characteristics. These filters are commonly used in aerospace certification and based on empirical data, see, e.g., [12].

The turbulence filter (24) and (25) require a white noise input to produce adequate disturbance. Directly applying these two filters in the LTV analysis will not yield feasible results as the $L_2[0,T]$ to $\|e(T)\|_2$ considers any norm bounded input signal. Hence, wind filters applied in the LTV analysis must convert any $L_2[0,T]$ bounded signal into a signal with spectral characteristics comparable to realistic turbulence. Specifically, the design procedure shall provide wind filters to provide worst-case wind signals matching the original turbulence fields' power spectral density (PSD).

The proposed design procedure consists of three steps and is exemplary shown for the longitudinal turbulence shaping filter. First, 2000 random turbulence profiles are generated along the reference approach trajectory by filtering unique white noise through (24). A sampling rate of 20Hz is used for the noise signal. The generated signals are limited to the finite time horizon $[0,T]$ defined by the time span of the reference approach. The second step is calculating the PSDs $\Omega_{u_{\mathrm{w},i}}$ of the time-domain wind signals $u_{\mathrm{w},i}$ using the average squared of their Fourier transform:

$$\Omega_{u_{\mathrm{w},i}}(\omega) = \lim_{T\to\infty} \frac{2}{\pi}\frac{1}{T}\left|\int_0^T u_{\mathrm{w},i}(t)e^{-j\omega t}dt\right|^2. \tag{26}$$

In this paper, the wind signals' Fourier transforms are calculated via a fast Fourier transform applying the built-in Matlab function `fft` for the finite time horizon $[0,T]$. Thirdly, a minimum phase first-order transfer function is calculated upper bounding the calculated $\sqrt{\left|\Omega_{u_{\mathrm{w},i}}(\omega)\right|}$ of all wind signals using Matlab's `fitmagfrd` function and a safety margin of 8dB. The latter accounts for the finite amount of considered wind signals and an immanent probability of exceedance for any statistically derived wind turbulence intensity, see e.g. [9]. As the analysis is conducted in the time domain, the transfer function is transformed into the LTI state-space representation $G_{u_w,\mathrm{LTV}}$. The subscript LTV emphasizes the filter's application in the LTV analysis. The PSD magnitudes for a selection of $u_{\mathrm{w},i}$ and the fitted wind filter $G_{u_\mathrm{w},\mathrm{LTV}}$ are compared in Fig. 6. As the longitudinal and lateral turbulence have the same spectral characteristics, this wind filter is also used in the lateral analysis. To increase clarity, it will be denoted as $G_{v_\mathrm{w},\mathrm{LTV}}$ in the lateral touchdown analysis. The turbulence wind filter for the vertical turbulence filter $G_{w_\mathrm{w},\mathrm{LTV}}$ is calculated accordingly.

3.4. Uncertainty Model

Aircraft and environmental parameters varying from the reference scenario result in different aircraft dynamics and approach trajectories. Hence, the corresponding aircraft LTV models differ from the nominal case in Section 3.2. Additionally, the trajectory has a direct influence on the linearized longitudinal/lateral controller's parameter further altering the closed loop dynamics. This is emphasized by the bode magnitude plot in Fig. 7. It shows transfer functions

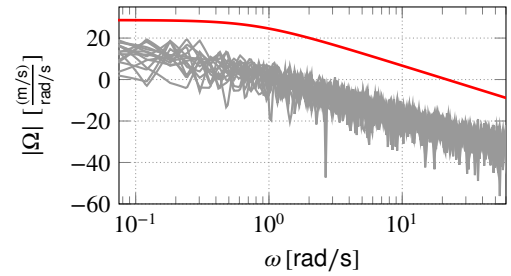

Figure 6: Comparison of the power spectral density magnitudes: LTV wind filter $G_{u_\mathrm{w},\mathrm{LTV}}$ (——), Monte Carlo turbulence signals $u_{\mathrm{w},i}$ (——)

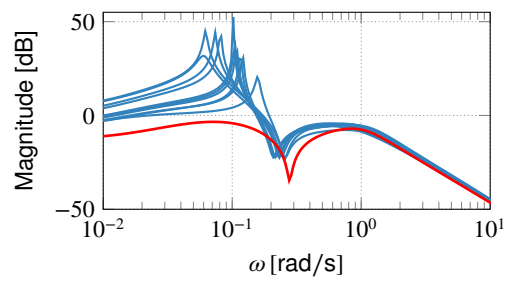

Figure 7: Bode magnitude plot of δ_e to α transfer functions calculated 10m above ground: nominal model (——), perturbed models (——)

from δ_e to α calculated at a frozen point in time corresponding to an altitude of 10m above ground level for different parameter combinations derived from the distributions provided in Tab. 2. Covering all uncertain parameters from Tab. 2 explicitly would result in an extensive IQC parameterization. Thus, for the lateral and longitudinal worst case analysis, all uncertain parameters are lumped into LTV weighted uncertainties Δ_long and Δ_lat of the following structure:

$$G_\mathrm{long} = (1 + W_\mathrm{long}\Delta_\mathrm{long})G_\mathrm{long,nom} \tag{27}$$

$$G_\mathrm{lat} = (1 + W_\mathrm{lat}\Delta_\mathrm{lat})G_\mathrm{lat,nom}. \tag{28}$$

In (27) and (28), Δ_long and Δ_lat are LTI uncertainties, with $\left\|\Delta_\mathrm{long}\right\|_\infty \leq 1$ and $\left\|\Delta_\mathrm{lat}\right\|_\infty \leq 1$, respectively, and W_long and W_lat are time-varying shaping filters. The weighting filters W_long and W_lat are calculated following the procedure proposed in [11]. Firstly, aircraft and controller LTV models for 200 approaches are calculated based on the parameter set in Tab. 2 and a selected static wind profile, i.e. a 25 kts side wind shear superimposed with either a 30 kts head wind or 10 kts tail wind shear. Secondly, on a frozen altitude grid spanning from 300 m to 0 m with 2.5 m step size, third-order minimal phase weightings are calculated such

that all closed-loop models are included in the uncertainty set (27) and (28), respectively. Afterwards, the altitude grid is mapped to the corresponding nominal approach trajectory's time grid. The corresponding time-varying weighting filters are obtained by piece-wise cubic Hermite polynomial interpolation. Note that separate weighting filters have to be calculated for each wind scenario presented in Section 3.3.

Note that the applied dynamic uncertainty adds conservatism to the worst-case analysis compared to an explicit parametric uncertainty set. However, this drawback is of theoretical nature, as a parametric uncertainty set based on Tab. 2 results in a large IQC parameterization. This large parameterization makes the problem harder to solve and in practice introduces conservatism to the result. An IQC analysis also does not provide the worst-case uncertainty combination. Hence, the analysis would not provide additional information, but only increase the computational time significantly. Moreover, given the worst-case nature of the analysis the increase in conservatism compared to the Monte Carlo simulation can be seen as beneficial.

The dynamic uncertainty description also mitigates the fact that LTV analyses can only handle a predefined analysis horizon, which is an inherent limitation of the LTV IQC framework, see, e.g., [22]. However, the static wind scenarios as well as varying environmental and aircraft parameters influence the approach duration in a deterministic fashion (as it is the case for the reference approach). Therefore, these parameters influence the touchdown performance mainly by altering the aircraft dynamics at specific times. Given the deterministic nature, certain times map to certain altitudes above ground level. The proposed weight calculation over a frozen altitude grid exploits this correlation. Converting the altitude dependent weights then back to the time grid of the respective reference approach scenario yields an uncertain LTV model defined over the predefined analysis horizon. This model covers the altitude-dependent dynamics of all considered approaches and their influence on the touchdown performance independently of their actual duration.The wind turbulence for a given static head- or tailwind scenario does not significantly influence the touchdown time in the present paper. This small effect comes from the turbulence's stochastic nature and was confirmed in extensive test scenarios.

4. Analysis

4.1. Analysis Scenarios

The analysis is tailored to give fast feedback in the controller's design process regarding the worst-case touchdown conditions. A summary of the different analyzed wind scenarios introduced in Section 3.3 and corresponding touchdown conditions is given in Tab. 3. The first two wind scenarios asses the controller's performance in the pitch plane. They evaluate the landing gear's vertical velocity $V_{z,\mathrm{TD}}$ at touchdown and the landing gear's altitude above runway 60 m behind the threshold H_{60}. For each of the two scenarios, an individual reference trajectory is calculated based on the respective static wind condition as given in Tab. 3.

Table 3
Wind scenarios covered in the analysis

Case	Model	Static Wind [kts] Long.*	Static Wind [kts] Lat.	Turbulence	Criteria
1	Long.	+10	25	σ_u, σ_w	$V_{z,\mathrm{TD}}$, H_{60}
2	Long.	−30	25	σ_u, σ_w	$V_{z,\mathrm{TD}}$, H_{60}
3	Lat.	+10	25	σ_v	$y_{\mathrm{LG,TD}}$, $\beta_{\mathrm{LG,TD}}$, ϕ_{TD}
4	Lat.	−30	25	σ_v	$y_{\mathrm{LG,TD}}$, $\beta_{\mathrm{LG,TD}}$, ϕ_{TD}

* positive/negative value indicates tailwind/headwind

Additionally, both scenarios include horizontal and vertical turbulence. Note that for the H_{60} evaluation the final time in LTV analysis does not correspond to the reference trajectory's touchdown, but to the time the aircraft is 60 m behind the runway threshold.

The final two scenarios are assessing the controller's lateral performance. They evaluate the landing gear's lateral offset $y_{\mathrm{LG,TD}}$ and the sideslip angle $\beta_{\mathrm{LG,TD}}$ of the landing gear relative to the centerline, and the bank angle ϕ_{TD} at touchdown. As for the longitudinal scenario, the two considered reference trajectories consider the tail- and headwind case as specified in Tab. 3. The lateral scenarios only include turbulent crosswind.

4.2. Analysis Setup

The LTV worst-case longitudinal and lateral touchdown conditions are calculated applying the algorithm proposed in [7] on the nonlinear optimization problem (15). The former evaluates the uncertain closed loops G_{long} (head- and tailwind scenario, respectively) extended with the longitudinal and vertical wind filter $G_{\mathrm{w}_u,\mathrm{LTV}}$ and $G_{\mathrm{w}_w,\mathrm{LTV}}$, respectively. The latter evaluates the uncertain closed loops G_{lat} (head- and tailwind scenario, respectively) extended with the lateral wind filter $G_{v_{\mathrm{w}},\mathrm{LTV}}$. These uncertain representations must be transferred into the IQC framework to apply the analysis algorithm. In the first two test cases concerning the pitch plane, Δ_{long} is a 2×2 full block, dynamic LTI uncertainty. Its input/output behavior is covered by the IQC described in Example 1, with $n_v = n_w = 2$. A MacMillan degree ν of one is chosen, and the value of ρ is -1.25. This means $\Delta \in IQC_1(\Psi_1, M_1)$, with M_1 restricted to the set $\mathcal{M} := \{M = \begin{bmatrix} X \otimes I_2 & 0 \\ 0 & -X \otimes I_2 \end{bmatrix} : X = X^T \geq 0 \in \mathbb{R}^{2\times 2}\}$ and $\Psi_1 = \begin{bmatrix} \psi_1 \otimes I_2 & 0 \\ 0 & \psi_1 \otimes I_2 \end{bmatrix}$.

The same class of IQC is used to cover the input/output behavior of the SISO, dynamic LTI uncertainty Δ_{lat} in the lateral analysis. Here, $n_v = n_w = 1$, with the IQC factorization defined by $\nu = 1$ and $\rho = -0.75$. Hence, $\Delta \in$

$IQC_2(\Psi_2, M_2)$, with M_2 restricted to the set $\mathcal{M} := \{M = \left[\begin{smallmatrix} X & 0 \\ 0 & -X \end{smallmatrix}\right] : X = X^T \geq 0 \in \mathbb{R}^{2\times 2}\}$ and $\Psi_2 = \left[\begin{smallmatrix} \psi_2 & 0 \\ 0 & \psi_2 \end{smallmatrix}\right]$.

The finite horizon worst-case $L_2[0, T]$ to Euclidean gain only bounds the performance output signal's Euclidian vector norm over the disturbance inputs at the final time T. Therefore, for a given scenario, each touchdown condition must be evaluated separately. Thus, the LTV worst-case gain optimization has to be executed ten times (five individual criteria, each evaluated for two wind scenarios). A single analysis covering all touchdown conditions for a given wind scenario is not sufficient. Given the worst-case gain's definition, these analyses cannot identify the actual worst-cases of the single touchdown conditions.

The worst-case gain optimization algorithm applies a tailored logarithmically scaled adaptive differential evolution with linear population size reduction. The algorithm is initialized with an initial population size of 40 in the longitudinal analysis and 20 in the lateral analysis. The population size determines the set of initial guesses for the solution vector, i.e. feasible IQC paramterizations. Hence, the longitudinal analysis's larger IQC parameterization reasons the larger initial population size. In general, a factor of twenty per n_w provides fast and accurate optimization result. A total of 10 population iterations are conducted with a minimum population size of four, i.e. at least four guesses for the IQC parameterization are evaluated in each iteration. The logarithmic search space's lower and upper bound are set to -7 and 1, respectively. These bounds correspond to a decimal search space from 10^{-7} to 1. The limits are chosen sufficiently large such that no solution vector approaches the boundary. All other settings concerning the meta-heuristic are identical to the standard settings proposed in [7] and in general require no user adjustments.

To validate the worst-case analyses, four separate Monte Carlo simulations are performed, one for each wind scenario. Recall that these wind scenarios correspond to the vertices of the analysis in [3]. Each test case is covered by 10000 samples derived from Tab. 2 using the high fidelity model provided in [3].

4.3. Results

The LTV worst-case analysis calculated a maximum vertical touchdown velocity of $V_{z,\mathrm{TD,WC}_1} = 6.36\,\mathrm{m/s}$ and a minimal altitude above ground level 60 m behind the threshold H_{60} of 1.9 m for the tailwind scenario (i.e., scenario 1). The most critical touchdown conditions found in the respective Monte Carlo simulations are $V_{z,\mathrm{TD,MC}_1} = 4.79\,\mathrm{m/s}$ and $H_{60,\mathrm{MC}_1} = 2.25\,\mathrm{m}$.

In the headwind scenario (i.e., scenario 2), the worst-case vertical touchdown velocity of 7.44 m/s, and a worst-case H_{60,WC_2} of -6.40 m were calculated. Note that the value of H_{60,WC_2} is the difference between the reference altitude and the calculated worst-case altitude disturbance. Hence, a negative sign indicates that the landing gear touched the ground earlier than 60m from the threshold. The corresponding Monte Carlo simulation provided a critical $V_{z,\mathrm{TD,MC}_2}$ of 6.89 m/s and a H_{60}, MC_2 of -0.48 m. Hence, at least one short landing occurred, as the LTV analysis predicted. All previously discussed results, including the reference touchdown conditions, are summarized in Tab. 4. The "Reference" entry corresponds to the touchdown conditions of the reference approach.

Table 4
Longitudinal analysis

Analysis	Test Case 1		Test Case 2	
	$V_{z,\mathrm{TD}}$[m/s]	H_{60}[m]	$V_{z,\mathrm{TD}}$[m/s]	H_{60}[m]
Reference	1.37	13.25	1.49	4.7
LTV WC	6.36	1.9	7.44	−6.40
Monte Carlo	4.79	2.25	6.89	−0.48

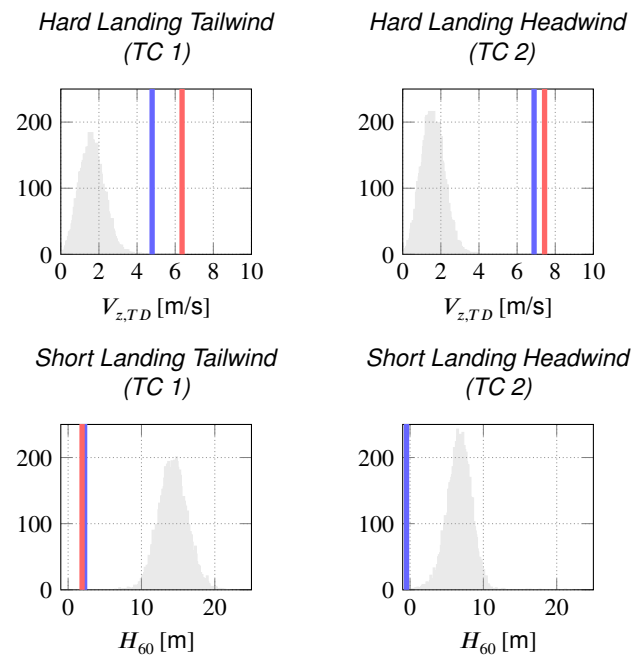

Figure 8: Analysis Results: LTV worst-case analysis (—), histogram Monte Carlo simulation (—), most critical Monte Carlo results(—)

In the following paragraphs, the lateral touchdown conditions are evaluated. For the third scenario (10 kts tailwind), the LTV worst-case analysis calculated a total bank angle at touchdown $\phi_{\mathrm{TD,WC}_3}$ of 11.29 deg, a lateral offset to the centerline $y_{\mathrm{LG,TD,WC}_3}$ of 11.4 m, and a worst-case sideslip angle of the landing gear $\beta_{\mathrm{LG,TD}_3}$ of 17.17 deg. Maximum values of 11.27 deg, 8.36 m, and 11.13 deg for the bank angle, lateral offset, and sideslip angle, respectively, were identified in the corresponding Monte Carlo simulation. For the fourth scenario (30 kts headwind), the LTV worst-case analyses calculated a total value of 11.01 deg for the bank angle, 14.46 m for lateral offset, and 17.61 deg for the sideslip angle. The corresponding Monte Carlo simulation's results

Table 5
Lateral analysis

Analysis	Test Case 3			Test Case 4		
	ϕ_{TD} [deg]	$y_{LG,TD}$ [m]	$\beta_{LG,TD}$ [deg]	ϕ_{TD} [deg]	$y_{LG,TD}$ [m]	$\beta_{LG,TD}$ [deg]
Reference	0.02	−0.90	0.97	0.21	1.39	1.39
LTV WC	11.29	11.40	17.17	11.01	14.46	17.61
Monte Carlo	11.27	8.36	11.13	10.72	13.42	16.37

are 10.72 deg for the bank angle, 13.42 m for the lateral offset, and 16.37 deg for the sideslip angle. In Tab. 5, the lateral analysis' results, as discussed, are summarized. Thus,

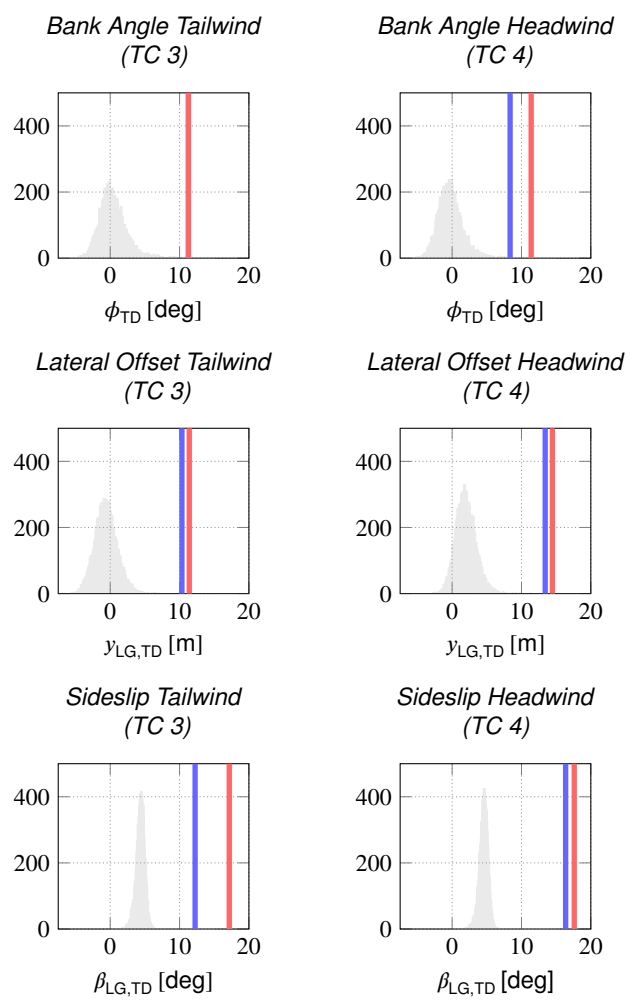

Figure 9: Analysis Results: LTV worst-case analysis (——), Histogram Monte Carlo simulation (- - -), Most critical Monte Carlo results (——)

each Monte Carlo simulation is upper bounded by the respective LTV worst-case. This is visualized in Fig. 8 and Fig. 9, showing the four Mont Carlo analyses' histograms

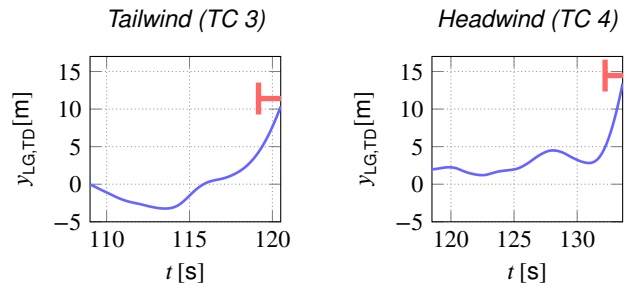

Figure 10: Comparison of lateral offset from flare initiation to touchdown: Most critical Monte Carlo result (——), LTV worst-case bound (|——)

with their most critical value highlighted and the individual LTV worst-cases. Notably, the ten LTV analyses were completed in 80 min, which is eight times faster than the 640 min required for the four Monte Carlo simulations, given the relatively small sample size of 10000. Therefore, the LTV analysis is more viable to quickly assess the qualitative impact of design changes as is required in an iterative tuning process. Fig. 10 compares the most critical lateral offset to the centerline identified in the Monte Carlos simulation (during the flare segment) to the worst-case of the LTV analysis. The lateral deviation remains small at the beginning of the flare and increases rapidly before touchdown. This behavior results from the decrab maneuver. All analyses were run on a standard desktop computer equipped with an Intel i7 processor and 32GB memory. Furthermore, only the LTV worst-case analysis identifies (guaranteed) worst-cases, whereas the Monte Carlo simulation can only provide lower bounds on the touchdown conditions. Additionally, the distributions in Fig. 8 and Fig. 9 indicate that the latter requires large sample sizes to allow for meaningful conclusions on the most critical touchdown scenarios. Note that the Monte Carlo simulation results here are more conservative than those in [24], as the latter uses the original code provided in [3] for the touchdown evaluation. The original code applies turbulence intensities proportional to the maximum static wind velocities, whereas the Monte Carlo simulation in the present paper uses the maximum possible values of the turbulence intensities in every analysis.

5. Conclusion

The proposed linear time-varying analysis procedure of an autolanded aircraft provides fast upper bounds on the worst-case touchdown conditions under elaborate wind scenarios. Treating the aircraft as a finite horizon linear time-varying system, allows to respect the varying dynamics and changing control laws under the restriction of the approach's finiteness. As the linear time-varying results establish feasible upper bounds for the Monte Carlo simulations conducted on corresponding high-fidelity nonlinear model in a fraction of time, it provides a supplemental tool for the design process and evaluation of autolanding controllers.

References

[1] Airbus S.A.S, 2011. Safety first. techreport 12. Airbus S.A.S, Blagnac Cedex, France.

[2] Airbus S.A.S, 2020. A Statistical Analysis of Commercial Aviation Accidents1958-2019. Technical Report. Airbus S.A.S, Blagnac Cedex, France.

[3] Biannic, J.M., Boada-Bauxell, J., 2017. A Civilian Aircraft Landing Challenge. Technical Report. ONERA. Toulouse. On-line available from the aerospace benchmark section of the SMAC Toolbox, http://w3.onera.fr/smac.

[4] Biannic, J.M., Roos, C., 2015. Flare control law design via multichannel H_∞ synthesis: Illustration on a freely available nonlinear aircraft benchmark, in: 2015 American Control Conference (ACC), IEEE. doi:10.1109/acc.2015.7170913.

[5] Biertumpfel, F., Pfifer, H., 2018. Worst case gain computation of linear time-varying systems over a finite horizon, in: 2018 IEEE Conference on Control Technology and Applications (CCTA), IEEE. doi:10.1109/ccta.2018.8511591.

[6] Biertümpfel, F., Pfifer, H., Bennani, S., 2019. Finite horizon worst case analysis of launch vehicles. IFAC-PapersOnLine 52, 31–36. doi:10.1016/j.ifacol.2019.11.065.

[7] Biertümpfel, F., Pholdee, N., Bennani, S., Pfifer, H., 2021. Finite horizon worst-case analysis of linear time-varying systems applied to launch vehicle. Manuscript submitted for publication .

[8] Boeing, 2018. Statistical Summary of Commercial Jet Airplanes Accidents 1959–2017. Technical Report. The Boeing Company. Worldwide Operations, Seattle, Washington,D.C.

[9] EASA, 2018. Easy Access Rules for All Weather Operations (CS-AWO). Technical Report. European Union Aviation Safety Agency, Cologne, Germany.

[10] Green, M., Limebeer, D.J.N., 1995. Linear Robust Control. Prentice-Hall, Inc., Upper Saddle River, NJ, USA.

[11] Hindi, H., Seong, C.Y., Boyd, S., 2002. Computing optimal uncertainty models from frequency domain data, in: Proceedings of the 41st IEEE Conference on Decision and Control, 2002., IEEE. doi:10.1109/cdc.2002.1184290.

[12] Hoblit, F.M., 1988. Gust Loads on Aircraft: Concepts and Applications. American Institute of Aeronautics and Astronautics. doi:10.2514/4.861888.

[13] ICAO, 2018. ICAO Safety Report 2018 Edition. Technical Report. International Civil Aviation Organization, Montreal, Canada.

[14] Ji, H., Chen, R., Li, P., 2017. Analysis of helicopter handling quality in turbulence with recursive von kármán model. Journal of Aircraft 54, 1631–1639. doi:10.2514/1.c034189.

[15] Juang, J.G., Chien, L.H., Lin, F., 2011. Automatic landing control system design using adaptive neural network and its hardware realization. IEEE Systems Journal 5, 266–277. doi:10.1109/jsyst.2011.2134490.

[16] Kawaguchi, J., Ninomiya, T., Miyazawa, Y., 2011. Stochastic approach to robust flight control design using hierarchy-structured dynamic inversion. Journal of Guidance, Control, and Dynamics 34, 1573–1576. doi:10.2514/1.53257.

[17] Knoblach, A., Pfifer, H., Seiler, P.J., 2015. Worst case analysis of a saturated gust loads alleviation system, in: AIAA Guidance, Navigation, and Control Conference, American Institute of Aeronautics and Astronautics. doi:10.2514/6.2015-0858.

[18] Looye, G., Joos, H.D., 2006. Design of autoland controller functions with multiobjective optimization. Journal of Guidance, Control, and Dynamics 29, 475–484. doi:10.2514/1.8797.

[19] McRuer, D.T., Graham, D., Ashkenas, I., 1974. Aircraft Dynamics and Automatic Control. Princeton University Press.

[20] Pfifer, H., Seiler, P., 2016. Less conservative robustness analysis of linear parameter varying systems using integral quadratic constraints. International Journal of Robust and Nonlinear Control 26, 3580–3594. doi:10.1002/rnc.3521.

[21] Seiler, P., 2015. Stability analysis with dissipation inequalities and integral quadratic constraints. IEEE Transactions on Automatic Control 60, 1704–1709. doi:10.1109/tac.2014.2361004.

[22] Seiler, P., Moore, R.M., Meissen, C., Arcak, M., Packard, A., 2019. Finite horizon robustness analysis of LTV systems using integral quadratic constraints. Automatica 100, 135–143. doi:10.1016/j.automatica.2018.11.009.

[23] Tadmor, G., 1990. Input/output norms in general linear systems. International Journal of Control 51, 911–921. doi:10.1080/00207179008934104.

[24] Theis, J., Ossmann, D., Thielecke, F., Pfifer, H., 2018. Robust autopilot design for landing a large civil aircraft in crosswind. Control Engineering Practice 76, 54–64. doi:10.1016/j.conengprac.2018.04.010.

[25] Veenman, J., Scherer, C.W., Köroğlu, H., 2016. Robust stability and performance analysis based on integral quadratic constraints. European Journal of Control 31, 1–32. doi:10.1016/j.ejcon.2016.04.004.